Cell Genomics

Article

Spatial transcriptomics identifies novel *Pseudomonas aeruginosa* virulence factors

Graphical abstract

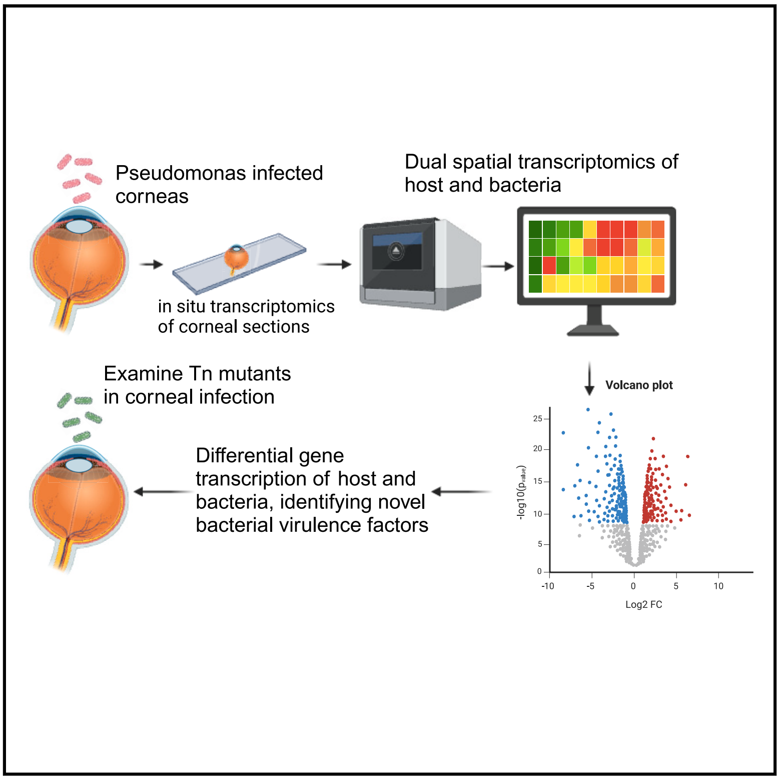

Authors

Hao Zhou, Oscar Negrón,
Serena Abbondante, ..., Obadiah Plante,
Eric Pearlman, Mihaela Gadjeva

Correspondence

eric.pearlman@uci.edu (E.P.),
mihaelagadjeva@gmail.com (M.G.)

In brief

Hao Zhou and colleagues uncover unique spatial patterns of gene activity by analyzing infected tissues. They combine spatial and transcriptional data to develop predictive analyses and identify bacterial genes that cause worse corneal disease. Overall, authors introduce a powerful approach for analyzing infection that could help predict new treatment strategies.

Highlights

- Spatial transcriptome analysis captures host and pathogen signatures
- Integrating spatial data allows the prediction of bacterial burden at infected sites
- Transcript enrichment analysis highlights virulence mechanisms

Zhou et al., 2025, Cell Genomics *5*, 100805
March 12, 2025 © 2025 The Author(s). Published by Elsevier Inc.
https://doi.org/10.1016/j.xgen.2025.100805

Cell Genomics

CellPress
OPEN ACCESS

Article

Spatial transcriptomics identifies novel *Pseudomonas aeruginosa* virulence factors

Hao Zhou,[1,2,4] Oscar Negrón,[2,5] Serena Abbondante,[3,5] Michaela Marshall,[3,5] Brandon Jones,[2] Edison Ong,[2] Nicole Chumbler,[2] Christopher Tunkey,[2] Groves Dixon,[2] Haining Lin,[2] Obadiah Plante,[2] Eric Pearlman,[3,6,*] and Mihaela Gadjeva[2,*]

[1]Department of Biological Sciences, College of Medicine and Health Sciences, Khalifa University, Abu Dhabi, United Arab Emirates
[2]Moderna, Inc., 325 Binney St., Cambridge, MA 02142, UK
[3]Department of Ophthalmology, School of Medicine, University of California, Irvine, 843 Health Sciences Rd., Irvine, CA 92697, USA
[4]Present address: Hao Zhou, Department of Biological Sciences, College of Medicine and Health Sciences, Khalifa University, Abu Dhabi, United Arab Emirates
[5]These authors contributed equally
[6]Lead contact
*Correspondence: eric.pearlman@uci.edu (E.P.), mihaelagadjeva@gmail.com (M.G.)
https://doi.org/10.1016/j.xgen.2025.100805

SUMMARY

To examine host-pathogen interactions, we leveraged a dual spatial transcriptomics approach that simultaneously captures the expression of *Pseudomonas aeruginosa* genes alongside the entire host transcriptome using a murine model of ocular infection. This method revealed differential pathogen- and host-specific gene expression patterns in infected corneas, which generated a unified transcriptional map of infection. By integrating these data, we developed a predictive ridge regression model trained on images from infected tissues. The model achieved an R^2 score of 0.923 in predicting bacterial burden distributions and identifying novel biomarkers associated with disease severity. Among iron acquisition pathogen-specific gene transcripts that showed significant enrichment at the host-pathogen interface, we discovered the novel virulence mediator PA2590, which was required for bacterial virulence. This study therefore highlights the power of combining bacterial and host spatial transcriptomics to uncover complex host-pathogen interactions and identify potentially druggable targets.

INTRODUCTION

Genomic and transcriptomic methodologies, including next-generation sequencing and high-throughput RNA analysis, open possibilities for characterizing the interactions between pathogens and their hosts. Traditionally, these approaches produce aggregate data from entire infected tissues.[1–3] However, missing from these analyses is spatial resolution, which can enhance our understanding of the bacterial and host response in infected tissues. We hypothesize that transcriptional analysis combined with spatial resolution will allow us to explore holistically how pathogens adapt and survive within specific tissue microenvironments. This approach also identified novel virulence factors that are potential targets for therapeutic intervention.

Recently, machine learning methods have been used to diagnose viral and bacterial infectious diseases[4,5] and to predict the risk of secondary bacterial infections.[6] These studies were performed on data acquired through microarray or RNA sequencing (RNA-seq) approaches using peripheral blood samples. These reports utilized a pretrained neural network model that showed a robust ability to distinguish among viral, gram-positive and gram-negative bacteria during acute infections.[5,7] The studies paved the way for integrated host transcriptome-based precision diagnosis but lack profiling of pathogen-specific responses.

RNA-seq approaches have been used to characterize host and pathogen transcriptomes either in independent experiments requiring integration analysis to combine the datasets or in the context of an intracellular infection.[8,9] To the best of our knowledge, machine learning has not been applied to connect host responses to pathogen transcripts in bulk RNA-seq experiments.

In contrast, the current study employs dual spatial transcriptomics profiling, a novel approach that captures the expression profiles of bacterial gene transcripts alongside the complete host transcriptome within infected tissues. This methodology was applied to examine the transcriptional landscape of *P. aeruginosa*-induced infection in a clinically relevant model of acute ocular disease. By mapping the pathogen-specific transcriptional profiles at a localized scale, we reveal temporal site-specific transcriptional adaptations and novel virulence factors. This approach also uses spatial data to identify novel bacterial virulence factors in a non-biased manner.

Cumulatively, our findings not only highlight the significance of integrating spatially resolved transcriptomic data to explore the complexities of host-pathogen interactions but also suggest

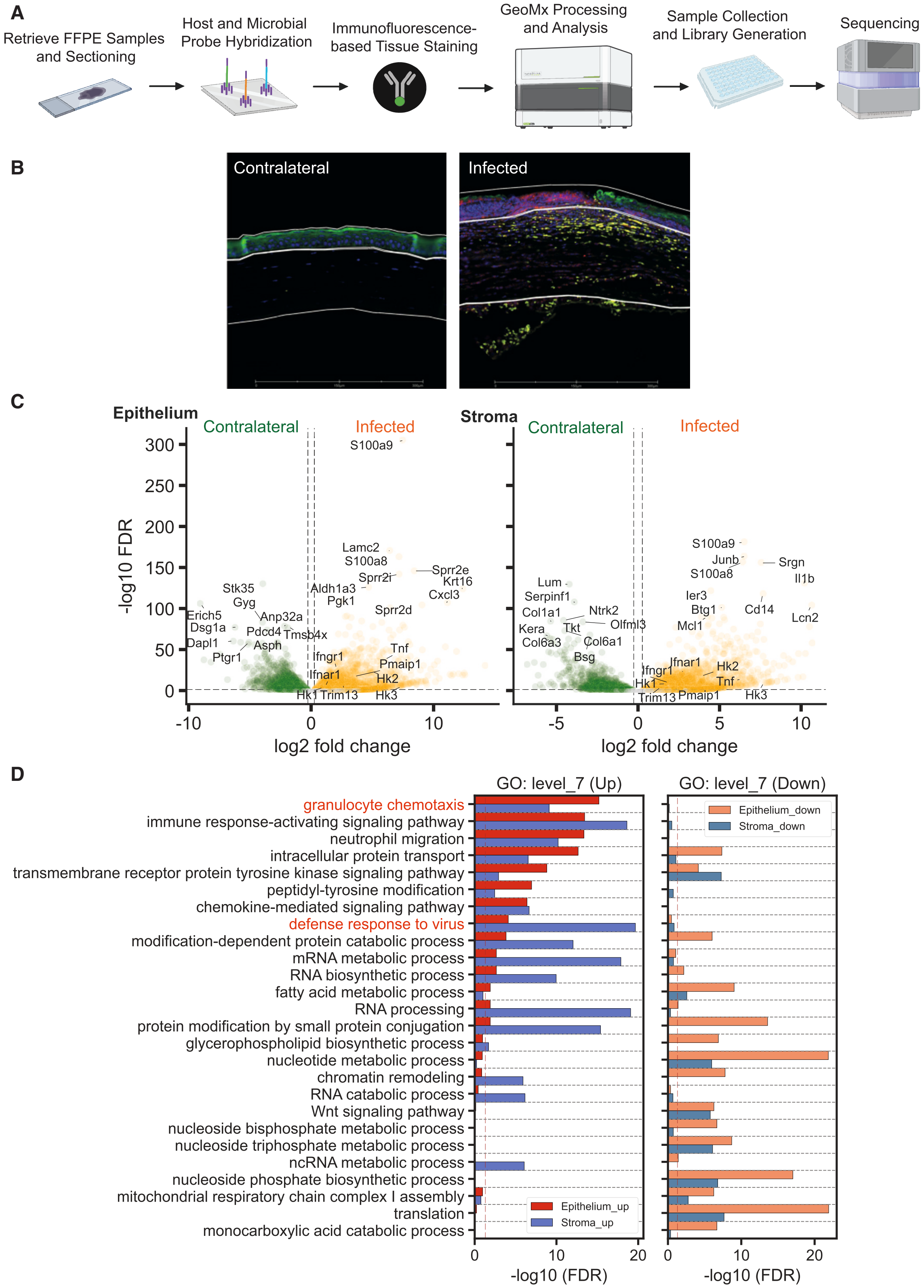

(legend on next page)

potential avenues for the development of targeted therapeutic interventions.

RESULTS

Spatial transcriptomics reveals tissue segment-specific host transcript enrichment

To generate a spatial transcriptional profile of infection, we used a well-characterized murine model of *P. aeruginosa* corneal infection. We utilized the Nanostring GeoMx platform for non-biased characterization of the host transcriptome (Figure 1A). Sections from paraffin-embedded eyes were processed, and we examined the responses in the corneal epithelium, the corneal stroma, and the anterior chamber as regions of interest (ROIs). The workflow is shown in Figure 1A.

Corneal epithelial cells were identified by expression of keratin 6, and neutrophils were identified using antibodies to Ly6G. Uninfected (contralateral eyes) and infected ocular tissues were examined (Figure 1B). Transcriptome analysis revealed common and segment-specific enrichment of host and bacterial transcripts. Consistent with the rich neutrophil infiltration into the infected tissues, *S100a8* and *S100a9* transcripts were highly upregulated in neutrophils in the epithelium and stroma (Figure 1C). Also upregulated were the neutrophil and monocyte chemokines *cxcl2*, and *ccl3*; the pro-inflammatory cytokines *il-1a*, *il-1b*, and *il-12a*; and the neutrophil iron-chelating gene *lcn2*. *cxcl2*, *ccl3*, *csf3*, *cxcr4*, *il-1b*, *il-1a*, and *il-12a* cytokine transcripts were higher in the epithelium relative to the stroma (Figure 1C). These data were reflected in the Gene Ontology (GO) enrichment analysis, showing stronger granulocyte chemotaxis enrichment in epithelium versus stroma.

In contrast, transcripts associated with RNA metabolism, processing, noncoding RNA processing, and chromatin remodeling were predominantly upregulated in the stromal layer when compared to epithelium. Surprisingly, the infected stroma showed elevated transcripts associated with anti-viral responses (Figure 1D), including type I interferon (IFN) and IFNAR1 and several IFN-induced transcripts (Table S1).

After 48 h, when there was elevated corneal opacity (Figures S1A and S1B), the epithelial layer displayed enrichment of transcripts associated with metabolic alterations, including glucose catabolism and cellular responses to glucose starvation, translation, and RNA (Figures S1C and S1D; Table S2). In the stroma, we found sustained enrichment of transcripts associated with neutrophil recruitment, glucose catabolism, pyruvate metabolism, and apoptosis (Figures S1C and S1D; Table S2). 24 and 48 h post infection, the global host transcriptome data showed a strong correlation between the individual biological replicas in the experiments (Figure S2). Cumulatively, our data provide a temporal transcriptional and spatial record of tissue alterations during infection that are associated with neutrophil cytokine production and metabolic changes.

Spatial analysis of bacterial transcript abundance in infected corneas reveals distinct enrichment profiles between the epithelium and stroma

Probes were generated for 100 *P. aeruginosa* genes that encode outer membrane proteins, extracellular proteins, reported virulence factors, and unknown predicted genes. Probe development was based on the criteria of open reading frame (ORF) frequency in >11,000 clinical isolates, evolutionary conservation, and their relation to known virulence factors. Three different gene-specific probes were designed for each of the bacterial genes of interest and used simultaneously to identify bacterial transcripts in the infected tissues (Table S3).

Transcript expression was examined in PAO1-infected corneal epithelium compared with the stroma and anterior chamber (AC). Representative images showed loss of the cytokeratin staining, consistent with the loss of epithelial cells and corneal perforation (ulceration) that occurs following infection. The underlying stromal layers showed Ly6G$^+$ staining, indicative of neutrophil infiltration to infected corneas (Figures 2A and 2B). Overall, we could distinguish ROIs with high or low bacterial transcripts. This was reflective of the number of bacteria at distinct sites in the infected eye. While 97 transcripts were detected at the corneal surface, only 37 transcripts were detected in most of the stromal segments. Interestingly, nine transcripts were consistently detected in the cytokeratin$^+$ and cytokeratin$^-$ surface layers, stromal regions with or without neutrophil, and in the AC, including

Figure 1. Non-biased whole-mouse transcriptome analysis of *P. aeruginosa*-infected tissues reveals differential enrichment for host transcripts depending on the anatomical site

(A) A schematic of the workflow. Ocular tissues were harvested 24 h post challenge with 1×10^6 CFUs of PAO1. Tissues were paraffin embedded, sectioned, stained for morphological markers, and hybridized with the whole host transcriptome probe library. ROIs were selected to encompass the epithelial layer, stromal layer, and AC of the eye. Probes were cleaved post hybridization, collected with GeoMx, and amplified, and the generated libraries were sequenced. The image was generated with BioRender.

(B) Representative immunohistochemical images of noninfected (contralateral control eyes) and *P. aeruginosa*-infected ocular tissues stained for cytokeratin (green), Ly6G (red), DNA (blue), and c-KIT (yellow) were visualized with GeoMx (scale bars, 300 μm; $n = 2$ biological replicas). Robust neutrophil infiltration (red) in the corneal stroma and epithelium is readily observed in the infected site.

(C) Volcano plots illustrating differentially expressed transcripts in epithelium and stroma tissue layers of the eye following infection compared to tissues of the non-infected contralateral eye 24 h post challenge. Data are presented cumulatively and derived from biological replicates. The analyzed tissue segments include 16 epithelial ROIs and 16 stromal ROIs collected from 2 biological replicas with 2 technical replicas each. The control contralateral ocular tissue analysis included 8 epithelial ROIs and 8 stromal ROIs from 2 technical replicas. The x axis indicates fold change (log2 scale), and the y axis shows the statistical significance (−log10 false discovery rate [FDR]-adjusted *p* values). Sample metadata are included.

(D) Bar plot of GO (Gene Ontology) functional enrichment analysis, highlighting tissue site-specific gene transcript clustering at level 7. The x axis displays the FDR-adjusted *p* values (−log10 scale), indicating the statistical significance of the enrichment. The y axis lists the level 7 GO categories with enriched transcripts. This analysis incorporates data from ROI profiles comprising 16 epithelial and 16 stromal samples from ocular tissues harvested 24 h post challenge ($n = 2$ biological replicas, $n = 2$ technical replicas per biological sample) and 8 epithelial and 8 stromal samples from control samples ($n = 2$, technical replicas). Data are presented cumulatively and are derived from biological replicates. GO enrichment analysis is listed in Table S1.

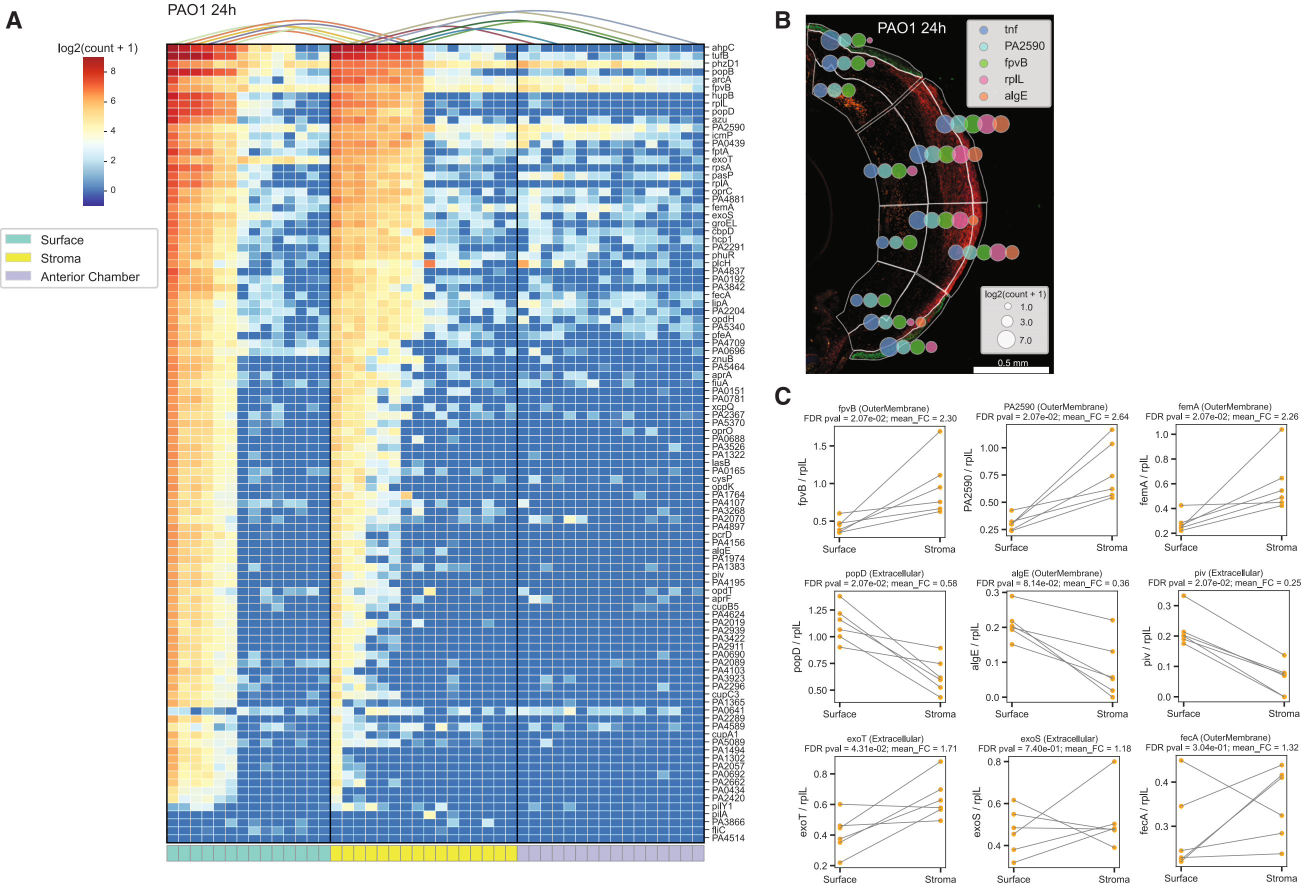

Figure 2. Bacterial transcript profiling of *P. aeruginosa*-infected corneas reveal differential tissue enrichment

(A) Heatmap showing the distribution of 100 bacterial transcripts in corneas infected with the *P. aeruginosa* ExoS-expressing strain PAO1. Each column represents data from individual ROIs. Data are presented cumulatively and derived from measurements of 2 biological and 2 technical replicas. Surface epithelial ROIs (*n* = 14 ROIs, *N* = 2 biological replicas, *n* = 2 technical replicas per biological sample) (green), stromal ROIs (*n* = 16 ROIs, *n* = 2 biological replicas, *n* = 2 technical replica per biological sample) (yellow), and anterior chamber (AC) ROIs (*n* = 16, *n* = 2 biological replicas, *n* = 2 technical replicas per biological sample) (purple) are grouped together. The curved lines at the top of the heatmap connect juxtaposing ROIs.

(B) Immunohistochemistry analysis of infected corneal sections stained for cytokeratin (green) and Ly6G+ neutrophils (red). Scale bar, 0.5 mm. Also shown is an overlay plot of host and bacterial transcript levels in PAO1-infected tissues. Logarithmic transcript abundances (log2(count + 1)) of host TNF-α and bacterial PA2590, F*fpvB*, *rplL*, and *a*AlgE are represented as circles, where the diameter reflects transcript numbers in the individual ROIs.

(C) Bacterial enrichment was calculated as relative transcript abundance in the surface segments compared to the stromal segments. Bacterial transcript levels were normalized to housekeeping bacterial *rRplL* transcripts. FDR values and fold change (FC) are annotated per gene. Representative bacterial enrichment data depict (1) transcripts that were enriched in the stroma *fpvB*, PA2590, and *femA*; (2) transcripts showing no enrichment; and (3) transcripts showing decreased abundance, such as *algE* and *piv*. Complete enrichment analysis is provided in Table S4.

ahpC, *tufB*, *phzD1*, *arcA*, *fpvB*, PA2590, *icmP*, *lipA*, and *femA* (Figures 2A and 2B).

Bacterial transcript enrichment analysis, normalized to the housekeeping *rplL* transcript abundance, reflected transcript increases in the infected stromal segments when compared to the infected surface layers (Figure 2C). Nineteen transcripts showed significant upregulation in the infected tissues (Table S4). Those included transcripts with known functions such as *arcA*, *phzD1*, *icmP*, *oprC*, *ahpC*, *lipA*, *exoT*, *phuR*, *opdH*, *fpvB*, and *femA* and transcripts encoding proteins that are predicted but have not been characterized: PA2590, PA0439, PA2204, PA2291, and PA4881. In contrast, transcripts for *algE*, *popD*, and *piv* were decreased in the stroma, while *exoS* and *fecA* showed no enrichment (Figure 2C; Table S4).

To determine whether bacterial transcript tissue penetrance is strain specific, corneas were infected with the cytotoxic (ExoU-expressing) PA14 strain. No significant enrichment of bacterial transcripts was observed at 24 h post challenge (data not shown); however, 48 h post challenge, deeper bacterial transcript penetrance and significant changes were detected (Figure 3A). The transcriptional heatmap comparisons between the sham and infected tissues confirmed the specificity of bacterial transcript detection (Figure 3A; Table S5). Fourteen transcripts were similarly enriched between the PA14 and PAO1 datasets. These included *phzD1*, *fpvB*, PA2590, *icmP*, *arcA*, *femA*, and *lipA* (Figures 3B–3D). Cumulatively, these results highlight the appearance of bacterial transcriptional patterns and spatial organization in infected tissues with ExoS- or ExoU-expressing strains.

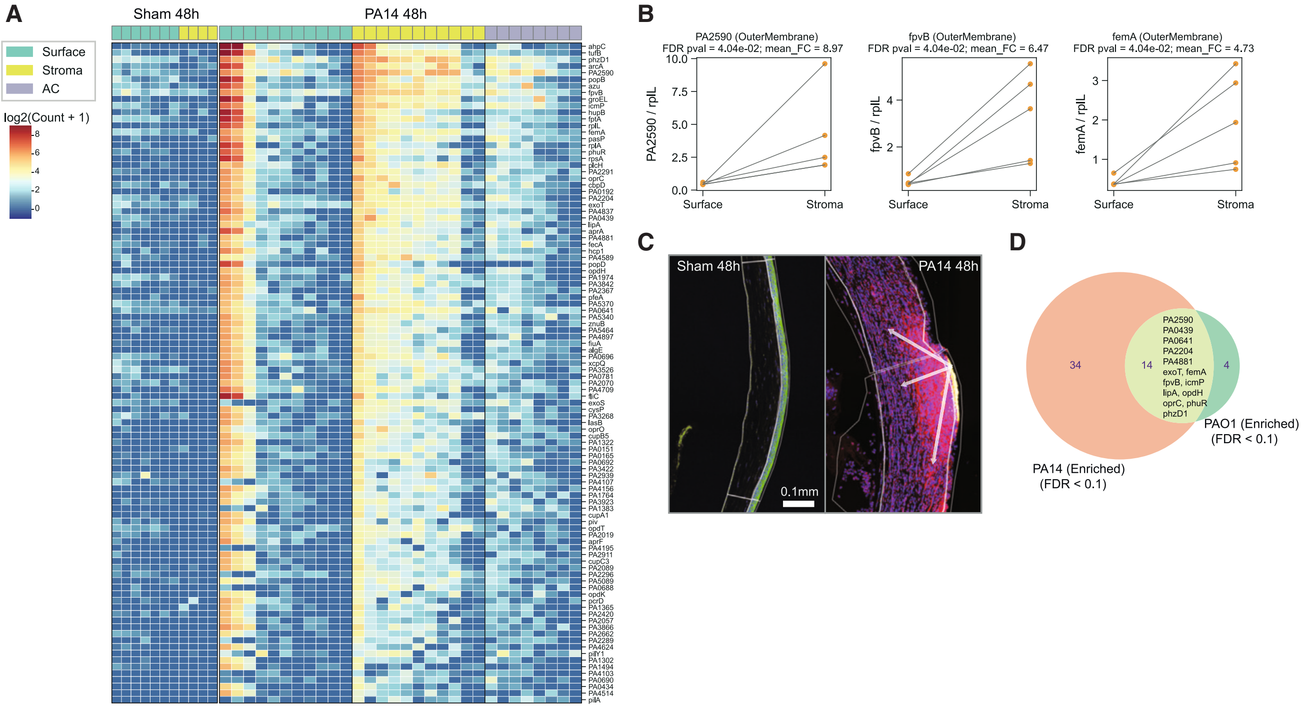

Figure 3. Bacterial transcript profiling of PA14-infected corneas

(A) Heatmap showing the distribution of 100 bacterial transcripts in uninfected and PA14-infected eyes. The sham (uninfected) and infected tissues were harvested and processed 48 h post challenge. Each column represents data from an individual ROI. Transcript abundance was compared between surface epithelial sham ROIs ($n = 6$ ROIs and $n = 2$ technical replicas) (green), stromal uninfected ROIs ($N = 4$ and $N = 2$ technical replicas) (yellow), and infected surface (epithelial) ROIs ($N = 11$ ROIs consisting of 2 or 3 surface ROIs per ocular section, $n = 3$ biological replicas and up to 2 technical replicas per biological sample) (green), infected stromal ROIs ($n = 11$ ROIs comprising 2 or 3 surface ROIs per ocular section, $n = 3$ biological replicas and up to 2 technical replicas per biological sample) (yellow), and infected AC ROIs ($n = 8$ consisting of 2 AC ROIs per ocular section and $n = 2$ biological replicas with 2 technical replicas per biological sample) (purple) are grouped together.

(B) Bacterial enrichment was calculated as relative transcript abundance in the surface (epithelial) segments compared to the stromal segments. Bacterial transcript levels were normalized to the housekeeping bacterial *rplL* transcripts. FDR values and FC are annotated for *fpvB*, PA2590, and *femA*. Complete enrichment analysis is provided in Table S5.

(C) Immunohistochemistry analysis of uninfected and PA14-infected corneal sections stained for OprI (yellow), cytokeratin (green), Ly6G+ neutrophils (red), and DNA (blue). Scale bar, 0.1 mm. Arrows indicate bacterial invasion from the surface lesion into the corneal stroma. Data are representative from sham ($n = 3$) and infected tissue ($n = 11$) biological replicates.

(D) Venn diagram depicting differentially present and shared bacterial transcripts that are enriched within the PAO1- and PA14-infected tissues. FDR values ≤ 0.1.

Harnessing host-bacterium dynamics for accurate prediction of infection levels in tissue regions

To examine the relationship between these newly identified genes, we compared their expression with the *P. aeruginosa* housekeeping gene *rplL*, which we used as a correlate for the number of bacteria in the infected tissues. Using ridge regression analysis (Figure 4A), we demonstrated significant predictive accuracy, achieving an R^2 score of 0.923. The selection of 800 key host gene transcript features (Figure 4B) refined the model, enhancing our understanding of the spatial distribution of bacteria in infected tissues.

We found that 150 host features were sufficient to accurately predict the number of bacteria in the cornea based on *rplL* transcript abundance, with an R^2 score of >0.8. We generated a host-bacterial *rplL* transcript correlation network and examined it for known host-protein interactions (Figure 4C). We found multiple signaling mediators associated with type I IFN, interleukin-1α (IL-1α), and tumor necrosis factor alpha (TNF-α)-driven inflammatory responses, which were highly interconnected for protein-protein interactions, further indicating that this host response network reflects coordinated immune mechanisms (Figure 4C). Examples of individual strong correlations between *P. aeruginosa rplL* and *tnfα*, *trim13*, and phorbol-12-myristate-13-acetate-induced protein1 (*pmaip1*) are shown (Figure 4D) and demonstrate that this approach can identify known (e.g., IL-1α and TNF-α) and unexpected immune determinants of infection, including Trim13 and Pmaip1. Employing "leave one out" validation of our model of corneas infected with PAO1 or PA14, as illustrated in Figure S3, showcases the adaptability of this approach and its potential for broad applicability. This approach also involves training the model on data from all but one host and assessing its predictive accuracy on the excluded host. The successful application of this technique across biological replicates demonstrates the model's robust predictive capacity.

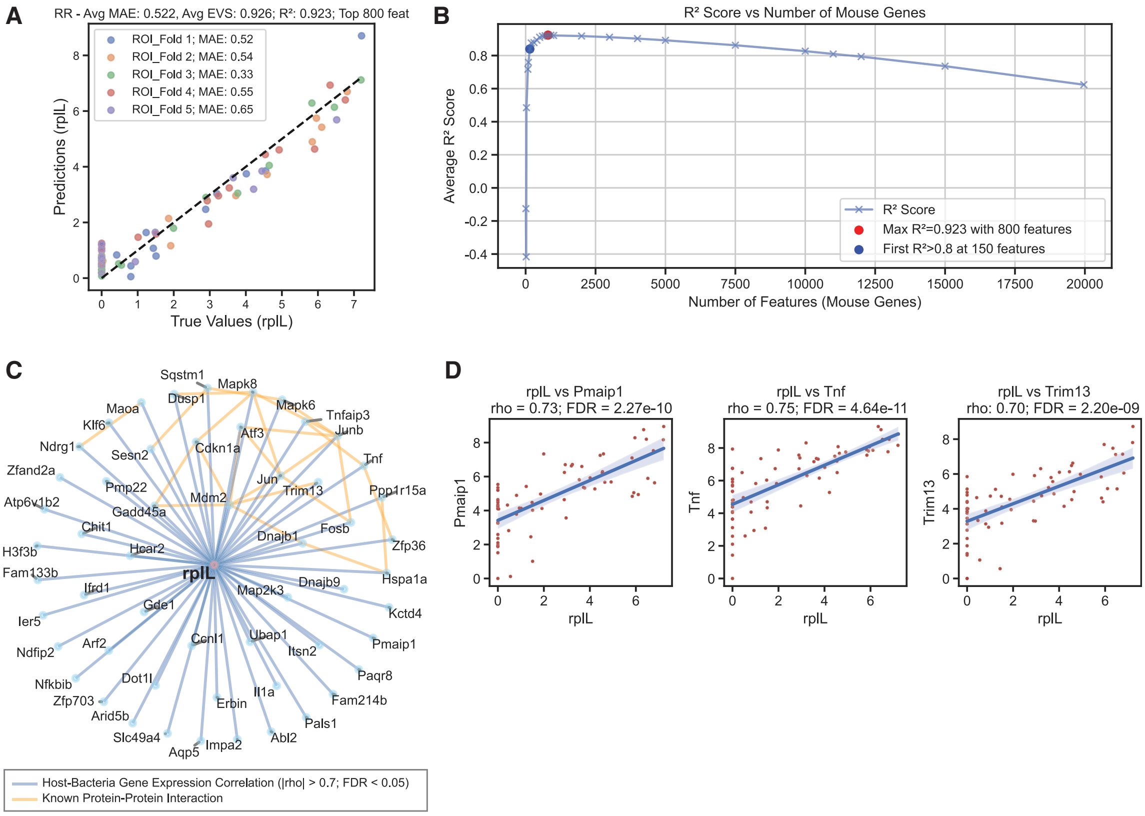

Figure 4. Harnessing host responses for highly predictive analysis of infection levels in tissue regions

(A) Residual plot of a ridge regression model trained on host expression profiles to predict bacterial *rplL* gene expression levels. Data values are transformed using log2(values + 1). The model underwent 5-fold cross-validation using ROIs from tissues 24 h post challenge. Model performance was evaluated based on average mean absolute error, explained variance score, and R^2 scores.

(B) Evaluation of model performance when trained with varying numbers of mouse gene features. Top features were chosen for subset training based on the coefficient values from the model trained using the complete dataset. Average R^2 scores provided the metric of assessment. Models, based on different feature sets, underwent optimization using grid search for hyperparameter tuning.

(C) Host-bacterium gene expression correlation network, including features with absolute rho values greater than 0.7 and an FDR less than 0.05, determined using Spearman's correlation.

(D) Correlative analysis showing bacterial rplL transcript abundance and host transcripts encoding TNF, pmaip, and Trim13 with absolute rho values greater than 0.7 and an FDR less than 0.05, determined using Spearman's correlation. The individual symbols represent values in tissue ROIs including surface epithelial sham ROIs ($n = 6$ ROIs and $n = 2$ technical replicas) (green), stromal sham ROIs ($n = 4$ and $n = 2$ technical replicas) (yellow), infected surface ROIs ($n = 11$ ROIs consisting of 2 or 3 surface ROIs per ocular section, $n = 3$ biological replicas, up to 2 technical replicas per biological sample) (green), infected stromal ROIs ($n = 11$ ROIs consisting of 2 or 3 surface ROIs per ocular section, $n = 3$ biological replicas, and up to 2 technical replicas per biological sample) (yellow), and infected AC ROIs ($n = 8$ consisting of 2 AC ROIs per ocular section, $n = 2$ biological replicas, 2 technical replicas per biological sample) (purple) grouped together. Data are presented cumulatively from ROI selections derived from biological and technical replicates described above.

Cumulatively, our approach offers a detailed perspective on the variability of bacterial load across tissue regions and demonstrates the ability to predict bacterial tissue burden by select host transcript feature abundance, thereby contributing to the field of precision medicine in diagnosing bacterial infections.

Transposon mutagenesis of PA2590 results in reduced virulence in infected corneas

Bacterial enrichment analysis identified known and unknown *P. aeruginosa* transcripts in *P. aeruginosa*-infected tissues. To determine whether there is any functional importance of the predicted PA2590 gene that showed significant penetrance in the infected tissues from PAO1- and PA14-challenged mice, corneas were infected with the *P. aeruginosa* PA14 wild-type (WT) parental strain or with a PA2590 transposon mutant (PA2590Tn). Infected eyes were imaged, and corneal opacity was imaged and quantified (Figure 5). We also assessed viable bacteria by colony-forming units (CFUs). Since we established similar transcriptional enrichment for PA2590 in the infected tissues of PAO1- and PA14-induced infections, infection studies were carried out with the PA14 strain.

There were no significant differences in corneal opacity or bacterial count between the WT PA14 strain and PA2590Tn 24 h post infection, consistent with the lack of enrichment for PA2590 at this data point (data not shown). However, after 48 h, corneas infected with the PA2590Tn mutant had less corneal opacity

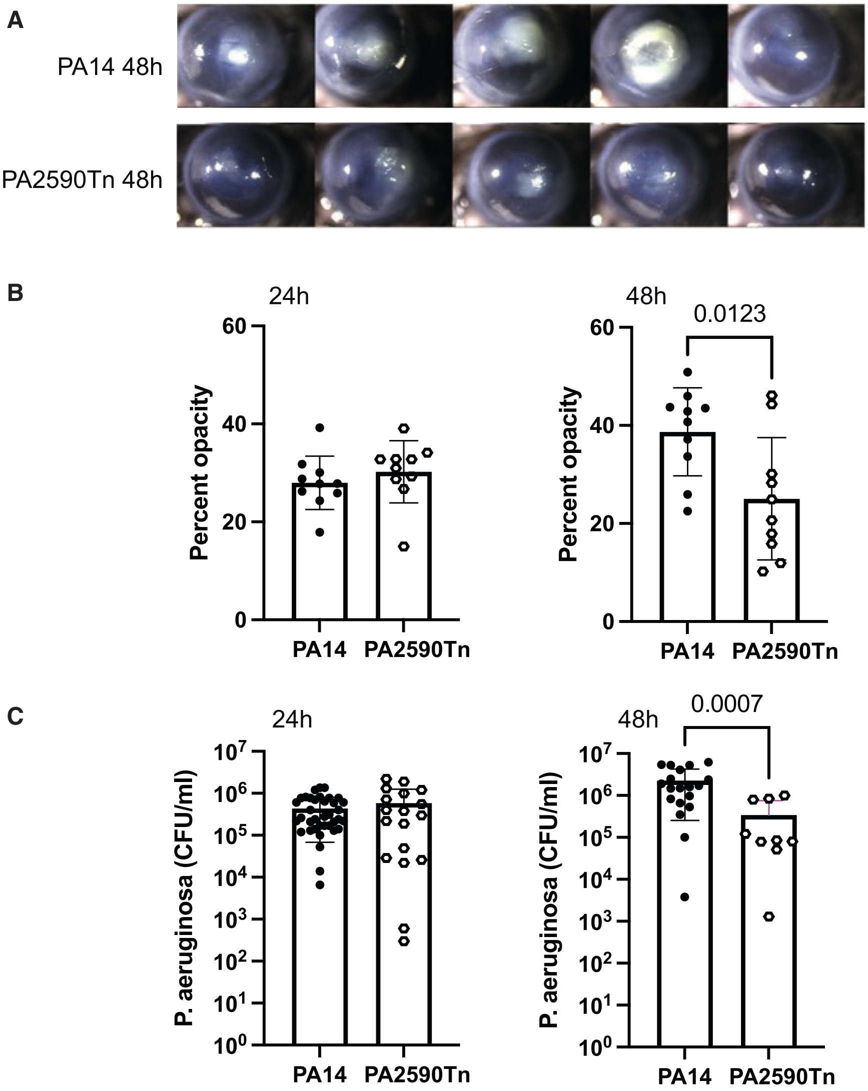

Figure 5. Infection with the PA2590Tn deletion mutant strain is associated with reduced pathology and bacterial burden

(A) Images from mice infected with PA14 (n = 5) and PA14 PA2590Tn deletion mutant mice (n = 5) were collected 48 h post challenge. Data represent one experiment of two performed.

(B) Corneal opacity scores reflective of disease severity were quantified by image analysis 24 and 48 h post challenge. Data are presented cumulatively from two independent experiments. The individual symbols present a single infected cornea. The filled symbols represent C57Bl6/J mice infected with the PA14 strain (n = 10), and the open circles represent C57Bl6/J mice infected with the transposon deletion mutant for PA2590 (n= 10). Data are represented as mean ± SD. Unpaired two-sided Student's t test with Welch's correction (p = 0.01).

(C) C57Bl6/J mice were infected with 5 × 10^5 CFUs of PA14 (n = 19) (filled circles) or with the PA14 PA2590Tn deletion mutant (n = 9) (open circles), and viable bacteria were quantified 24 and 48 h post challenge. Data are presented cumulatively from two independent experiments. The individual symbols present individual infected corneas. Data are represented as mean ± SD. Unpaired Student's t test with Welch's correction (p = 0.0007).

(Figure 5A) and significantly less bacteria when compared to with corneas infected with the parent PA14 strain (Figures 5B and 5C). As the bacterial burden at 48 h post-challenge is typically predictive of the disease outcomes in this model, we concluded that PA2590 is a *P. aeruginosa* virulence factor.

Structural comparison analysis suggests that PA2590 is an iron or vitamin B12 transporter

To identify a possible function of PA2590 in *P. aeruginosa* virulence, we used a bioinformatics approach to predict its prevalence, conservation, and structural properties. Analysis of PA2590 prevalence in 11,447 publicly available *P. aeruginosa* genomes derived from clinical isolates revealed that the PA2590 ORF is widely distributed and present in 97% of these clinical isolates (Figure 6A). There were no significant differences in PA2590 distribution based on geographic location. Amino acid conservation analysis was also performed using a library of genomes derived from clinical isolates from different clinical presentations of wounds, blood, lung, eye, and genitourinary tract infections (Figure S4). A high degree of conservation was identified in all isolates at the amino acid stretches encoding the extracellular loops of the predicted structure of PA2590 with AlphaFold2 (Figures 6B and S4B). Cumulatively, these data support our findings that PA2590 has an important biological function during infection.

Comparative structural analysis established a high degree of conformational similarities between PA2590 and the *E. coli* BtuB protein (PDB: 3m8d; R value free: 0.275) (Figure 6C). BtuB is a vitamin B12 (VB12) transporter, suggesting that PA2590 might have a similar function. Predicted docking experiments revealed that PA2590 is likely to bind VB12 (Figure 6E; Vina docking: −9.1 kcal/mol). This is similar to the docking score for the known VB12 binding proteins BtuB and VB12 (−8.2 kcal/mol). In addition to BtuB, our analysis identified structural homology between PA2590 and *E. coli* FepA (PDB: 1fep; R value free: 0.282) (Figure 6D). FepA is an iron and VB12 transporter.[10] The acquisition of iron depends on ferric enterobactin binding to FepA, where the transporter preferentially recognizes the catecholate part of the complex.[10] Unlike *E. coli*, our docking experiments did not indicate a potential interaction between enterobactin and PA2590. However, mammalian siderophores can be synthesized by eukaryotic homologs to the *E. coli* enzyme generating enterobactin.[11] Therefore, we examined the potential binding of PA2590 to an abundant host siderophore, 2,5-dihydroxybenzoic acid. Predicted *in silico* docking experiments confirmed the high

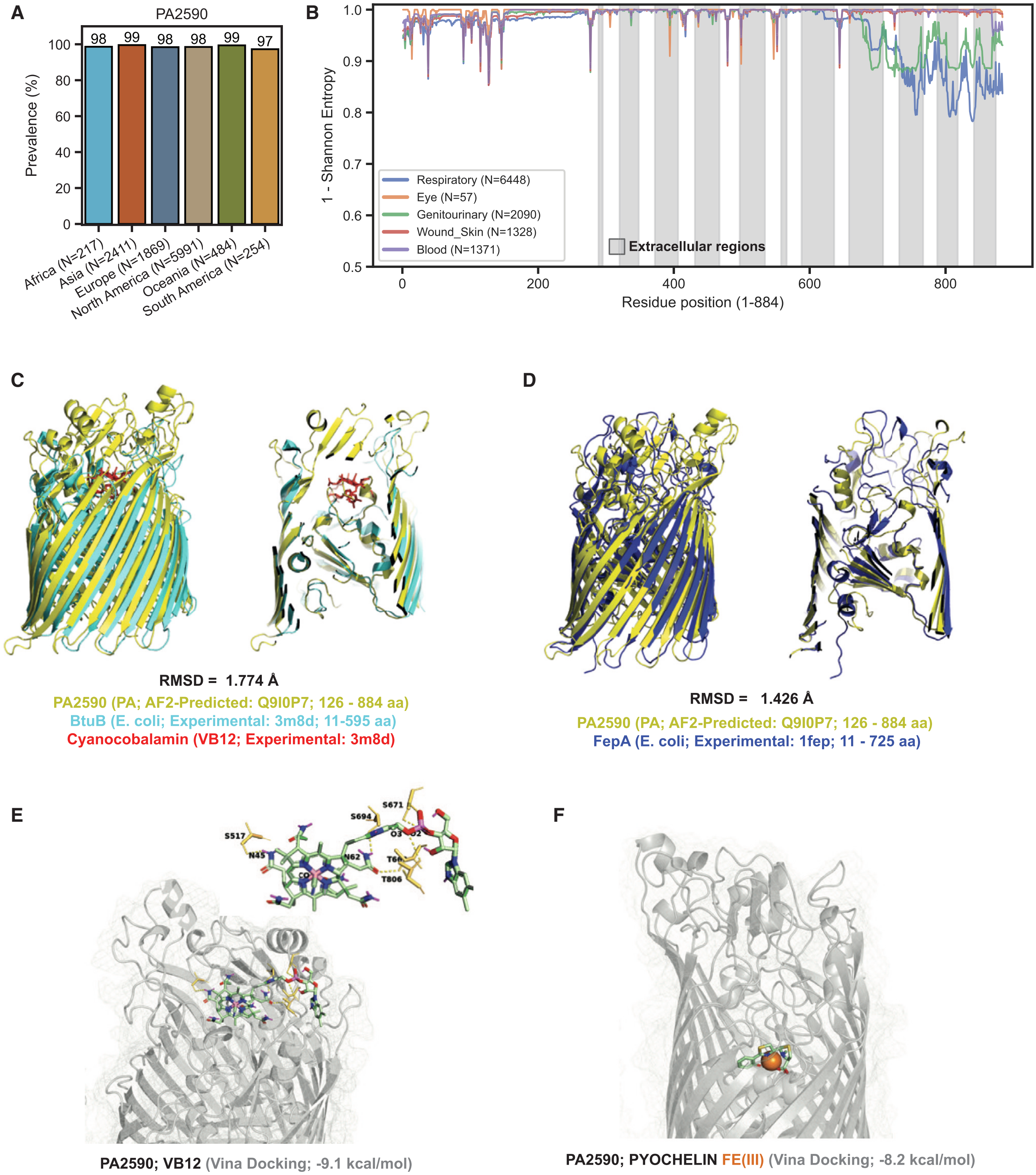

Figure 6. Structural homology analysis predicts the PA2590 gene to function as a VB12 and iron transporter

(A) Prevalence of the PA2590 gene in the genomes of *P. aeruginosa* clinical isolates sourced from multiple geographic regions: Africa (*N* = 216), Asia (*N* = 2,278), Europe (*N* = 1,680), North America (*N* = 5,763), Oceania (*N* = 366), and South America (*N* = 253). Here, *N* denotes the total number of clinical isolates analyzed from each region.

(B) Amino acid conservation analysis for the PA2590 gene, illustrating data from clinical isolates of *P. aeruginosa* obtained from different infection types: genitourinary (blue line, *N* = 1,991), respiratory (orange line, *N* = 6,132), blood (green line, *N* = 1,202), and wound/skin infections (red line, *N* = 1,302). The x axis displays the residue position, while the y axis shows the 1-Shannon entropy values. Shaded regions indicate the extracellular loops of the protein.

(legend continued on next page)

likelihood of this interaction (Figure S4C; Vina docking: −6.0 kcal/mol).

P. aeruginosa uses two main siderophores for iron uptake: pyoverdine and pyochelin.[12] As transcripts for both receptors were upregulated in the infected tissues, and to determine whether there might be redundancy in iron uptake, the potential interaction of PA2590 with Fe(III)-pyochelin was examined. The analysis showed a significant docking score of −8.2 kcal/mol, indicative of a role of PA2590 in the internalization of iron complexed with *Pseudomonas*-derived siderophores (Figure 6F). Cumulatively, our data indicate that PA2590 could mediate both iron and VB12 transport.

DISCUSSION

Bacterial infections remain a major global health threat, including those caused by *Pseudomonas aeruginosa*, a highly adaptable pathogen notorious for its resistance to antibiotics and its ability to cause severe infection in multiple tissues.[13,14] Despite its clinical significance, our understanding of the molecular mechanisms that underlie the ability of *P. aeruginosa* to thrive remains incomplete.[15,16] The complexity of host-pathogen interactions within infected tissues is a significant obstacle in developing effective therapies and vaccines.[17,18]

Spatial transcriptomic profiling of infected tissues provides information on gene expression patterns at specific infection sites. This report is the first to use dual spatial RNA-seq, combining bacterial pathogen-specific and host transcriptome data with spatial resolution into a unified, multidimensional dataset. This experimental approach represents a significant advancement over previous studies that used either sequential analysis of eukaryotic and prokaryotic features or reported bacterial analysis based only on 16S RNA-seq.[19,20] Our data illuminate differentially enriched bacterial transcripts at the host-pathogen interface, thereby identifying novel pathoadaptive mechanisms. The spatially resolved data enable machine learning approaches to connect host transcriptional networks with bacterial profiles, thereby identifying key nodes for targeted therapies.

Our study uncovered a strong predictive correlation between a network of interconnected host features and *P. aeruginosa* housekeeping transcript abundance (*rplL*) during infection. The choice of *rplL* was based on its use as a housekeeping gene for normalizing RT-qPCR data. Using at least 150 host features, we successfully predicted bacterial burden in each tissue segment with a significant degree of accuracy. The correlative analysis identified known and novel biomarkers of infection severity, including IL-1α, TNF-α, tripartite motif-containing 13 (TRIM13), Pmaip1, and Chit1. *P. aeruginosa* is a potent inducer of IL-1α and TNF-α , which orchestrate neutrophil infiltration to infected tissues.[19–21] Loss of IL-1α, unlike the loss of IL-1β, promotes resistance to infection.[22,23] Conversely, increases in IL-1α correlates with worse disease, illustrating that the Machine Learning-enabled analysis correctly identified IL-1α as a biomarker for *P. aeruginosa* disease severity. Novel biomarkers included increases in TRIM13 and phorbol 12-myristate 13-acetate-induced protein 1 (Pmaip1) transcripts.[24] These genes regulate autophagy and apoptosis,[25] and while direct studies linking Trim13 and Pmaip1 with *P. aeruginosa*-induced infection are lacking, their involvement in autophagy and apoptosis suggest mechanistic connections worth exploring in the future. The present study demonstrates the feasibility of this approach, and future analyses correlating host transcriptome features with other housekeeping genes or bacterial transcriptional programs will likely illuminate novel interaction networks.

We predicted that the bacterial transcriptional characteristics would show distinct features depending on anatomical location. Consistently, bacterial enrichment analysis exhibited a higher tissue penetrance of transcripts associated with iron acquisition. *P. aeruginosa* requires iron to detoxify reactive oxygen species and nitric oxide to ensure pathogen survival. *P. aeruginosa* has two major siderophores, pyoverdine and pyochelin, and the latter is essential for acute infection.[26] Transcripts for the pyoverdine receptor, f*pvB*, and the ferric mycobactin receptor, f*emA,* were significantly enriched during infection. In contrast, the pyochelin receptor, f*ptA*, did not show significant tissue enrichment, suggesting that there are other transporters for pyochelin import. To this end, we observed a significant penetrance of the PA2590 transcript encoding a predicted protein. Structural analysis showed that PA2590 has a 22-stranded antiparallel β barrel domain containing Ton B-dependent transporters and that PA2590 has a high degree of structural similarity to *P. aeruginosa* FemA transporters, indicating a possible role of PA2590 in mediating iron intake. Further docking analyses are indicative of pyochelin binding.

PA2590 is also structurally similar to a dual iron and VB12 transporter in *E. coli,* BtuB, suggesting that PA2590 has a role in cobalamin import.[27] The potential dual import of iron and VB12 reflects the ability of *P. aeruginosa* to survive in nutritionally poor, oxygen-limited environments.[28] Interestingly, *P. aeruginosa* synthesizes VB12 under aerobic conditions, although this activity is suppressed under anaerobic conditions.[29] The import system that facilitates anaerobic VB12 intake is presently unknown,[30] and our analysis offers insights into mechanisms of VB12 import.

(C) Structural homology modeling highlights parallels between the PA2590 structure predicted by AlphaFold2 and the structure of the *E. coli* BtuB protein. This contrasts with the predicted model (light green) of the Btub structure (dark green), with VB12 depicted in red. Superimposition of these structures was conducted using the cmd.align function in PyMOL, involving 1,000 alignment cycles with the transform parameter set to 1. This analysis resulted in a root-mean-square deviation (RMSD) of 1.774 Å for residues 126–884 of PA2590 and 11–595 of BtuB, indicating a significant level of structural similarity.

(D) Structural homology modeling highlights parallels between the PA2590 structure predicted by AlphaFold2 and the experimentally determined structure of the *E. coli* FepA protein. The predicted model (light green) and the FepA structure (dark blue) are depicted. The RMSD is 1.426 Å over amino acid residues 126–884 of PA2590 and 11–725 of FepA, indicating a significant degree of structural similarity.

(E) In silico docking experiments were conducted between PA2590 and VB12 using Autodock Vina. The pose with the lowest energy (kcal/mol) was chosen for representation. PyMOL scripts were used to highlight residues potentially interacting with PA2590, focusing on polar contacts within a 3.5 Å range.

(F) In silico docking experiments were conducted between PA2590 and pyochelin using Autodock Vina. The pose with the lowest energy (kcal/mol) was chosen for representation, indicating a docking score of −8.2 kcal/mol.

In *P. aeruginosa*, VB12-dependent enzymes, such as methylmalonyl-coenzyme A mutase,[31] methionine synthase,[32] ethanolamine ammonia-lyase,[33] glycerol dehydratase,[34] and diol dehydratase,[35] play crucial roles in metabolic versatility, which demonstrates the ability of these bacteria to use alternative carbon sources. VB12 also supports DNA replication under anaerobic conditions by serving as a cofactor for essential ribonucleotide reductases.[30] We also showed that PA2590 is functionally important in a clinically relevant model, *P. aeruginosa* corneal infection, as significantly less bacteria were recovered in the absence of PA2590. Cumulatively, these data demonstrate that this bioinformatics approach can identify novel pathoadaptation mechanisms, including bacterial virulence factors.

Our analyses highlight transcriptional changes associated with the host autophagy pathway and metabolite acquisition by the pathogen, which indicates a causative link between bacterial VB12, iron acquisition, and autophagy. Several reports show that iron sequestration by the host limits bacterial infection by promoting autophagy.[36–38] Additionally, iron-siderophore complexes incubated with *C. elegans* induce mitophagy, a form of damaged mitochondrial autophagy.[39] Conversely, inhibition of mitophagy renders *C. elegans* more susceptible to *P. aeruginosa*-induced infection.[39] VB12 deficiency, similar to iron starvation, promotes autophagy due to reduction in the citric acid cycle and ATP production.[40] Cumulatively, the spatially resolved data efficiently capture a complex host-pathogen interplay, identifying key metabolites, such as iron and VB12, that can regulate autophagy in the bacteria and can also mediate the host's resistance to infection.

In conclusion, the use of spatially resolved maps of infection is widely applicable to gain foundational insights into host-bacterial pathogen interactions that will guide future mechanistic research. Our spatial transcriptome data analysis approach identified novel virulence mechanisms associated with key requirements for pathogen survival during infection.

Limitations of the study

Given the extensive genomic diversity among *P. aeruginosa* isolates, expanding the analysis to investigate the biological role of PA2590 across different strains could provide valuable insights into potential strain-specific variability.

RESOURCE AVAILABILITY

Lead contact

The lead contact is Eric Pearlman, (eric.pearlman@uci.edu).

Materials availability

This study did not generate any unique materials.

Data and code availability

Raw transcript count data, original code, and associated imaging data have been deposited on Zenodo[41]:https://doi.org/10.5281/zenodo.14667250. The raw sequencing data have been submitted to NCBI GEO under accession number GEO: PRJNA1202130. Additionally, the code used for training predictive models and conducting correlative analyses is available on GitHub: https://github.com/modernatx/spatial_RNAseq_analyses and has also been archived on Zenodo: https://doi.org/10.5281/zenodo.14667250 for reproducibility.

ACKNOWLEDGMENTS

We would like to acknowledge the outstanding contributions of the NanoString team: Maxine Macclain, Espy Anguiano, Tim Riordan, Ozge Cagsal-Getkin, Mary Hentschel, and Ankush Tyagi, who worked tirelessly to help us conduct the feasibility studies and establish the technology. We would like to thank the University of Massachusetts Histopathology core, Yu Liu and Jayme Haywosz, for embedding and processing services. We would like to thank Prof. G. Pier (Mass General Brigham, Harvard Medical School) for providing the PA14 and PA14 PA2590 strains. This research was funded by Moderna and NIH EY14362 (to E.P.).

AUTHOR CONTRIBUTIONS

H.Z. conducted all computational analyses. S.A. and M.M. carried out all *in vivo* experiments and analyzed their results. O.N. was responsible for data acquisition within the GeoMx workflow. B.J. handled the sequencing analysis portion of the GeoMx workflow. M.G., E.O., and H.Z. selected the PA genes. C.T. advised on the sequencing aspects of the GeoMx workflow. G.D. and H.L. validated the PA2590 Tn mutant. M.G., H.Z., N.C., E.P., and S.A. played key roles in study design and data interpretation. M.G. devised the study concept, and contributed to data collection, analysis, and interpretation. H.Z., O.N., N.C., E.P., and M.G. drafted the initial manuscript. All authors discussed the data, reviewed, and revised the manuscript.

DECLARATION OF INTERESTS

H.Z., O.N., N.C., B.J., E.O., C.T., G.D., H.L., O.P., and M.G. are employees of Moderna Inc. and may hold stock/stock options in Moderna, Inc.

DECLARATION OF GENERATIVE AI AND AI-ASSISTED TECHNOLOGIES IN THE WRITING PROCESS

During the preparation of this work the author(s) used ChatGPT in order to proofread the text. After using this tool, the author(s) reviewed and edited the content as needed and take full responsibility for the content of the publication.

STAR★METHODS

Detailed methods are provided in the online version of this paper and include the following:

- KEY RESOURCES TABLE
- EXPERIMENTAL MODEL AND STUDY PARTICIPANT DETAILS
- METHOD DETAILS
  - Bacterial strains
  - Corneal opacity
  - Bacterial quantification
  - Ocular tissue processing
  - Spatial transcriptomics workflow
- QUANTIFICATION AND STATISTICAL ANALYSIS
  - Bacterial burden and opacity statistical analysis
  - Spatial transcriptome analysis
  - Predictive models and correlative analysis
  - PA2590 sequence analysis
  - Structural homology analysis and molecular docking

SUPPLEMENTAL INFORMATION

Supplemental information can be found online at https://doi.org/10.1016/j.xgen.2025.100805.

Received: September 30, 2024
Revised: November 22, 2024
Accepted: February 10, 2025
Published: March 12, 2025

REFERENCES

1. Pisu, D., Huang, L., Grenier, J.K., and Russell, D.G. (2020). Dual RNA-Seq of Mtb-Infected Macrophages In Vivo Reveals Ontologically Distinct Host-Pathogen Interactions. Cell Rep. *30*, 335–350.e4. https://doi.org/10.1016/j.celrep.2019.12.033.
2. Cornforth, D.M., Dees, J.L., Ibberson, C.B., Huse, H.K., Mathiesen, I.H., Kirketerp-Møller, K., Wolcott, R.D., Rumbaugh, K.P., Bjarnsholt, T., and Whiteley, M. (2018). Pseudomonas aeruginosa transcriptome during human infection. Proc. Natl. Acad. Sci. USA *115*, E5125–E5134. https://doi.org/10.1073/pnas.1717525115.
3. Harrington, N.E., Littler, J.L., and Harrison, F. (2022). Transcriptome analysis of Pseudomonas aeruginosa biofilm infection in an ex vivo pig model of the cystic fibrosis lung. Appl. Environ. Microbiol. *88*, e01789. https://doi.org/10.1128/aem.01789-21.
4. Mayhew, M.B., Buturovic, L., Luethy, R., Midic, U., Moore, A.R., Roque, J.A., Shaller, B.D., Asuni, T., Rawling, D., Remmel, M., et al. (2020). A generalizable 29-mRNA neural-network classifier for acute bacterial and viral infections. Nat. Commun. *11*, 1177. https://doi.org/10.1038/s41467-020-14975-w.
5. Xie, J., Zheng, X., Yan, J., Li, Q., Jin, N., Wang, S., Zhao, P., Li, S., Ding, W., Cheng, L., and Geng, Q. (2024). Deep learning model to discriminate diverse infection types based on pairwise analysis of host gene expression. iScience *27*, 109908. https://doi.org/10.1016/j.isci.2024.109908.
6. Carney, M., Pelaia, T.M., Chew, T., Teoh, S., Phu, A., Kim, K., Wang, Y., Iredell, J., Zerbib, Y., McLean, A., et al. (2024). Host transcriptomics and machine learning for secondary bacterial infections in patients with COVID-19: a prospective, observational cohort study. Lancet. Microbe *5*, e272–e281. https://doi.org/10.1016/S2666-5247(23)00363-4.
7. Li, Q., Zheng, X., Xie, J., Wang, R., Li, M., Wong, M.-H., Leung, K.-S., Li, S., Geng, Q., and Cheng, L. (2023). bvnGPS: a generalizable diagnostic model for acute bacterial and viral infection using integrative host transcriptomics and pretrained neural networks. Bioinforma. Oxf. Engl. *39*, btad109. https://doi.org/10.1093/bioinformatics/btad109.
8. Penaranda, C., Chumbler, N.M., and Hung, D.T. (2021). Dual transcriptional analysis reveals adaptation of host and pathogen to intracellular survival of Pseudomonas aeruginosa associated with urinary tract infection. PLoS Pathog. *17*, e1009534. https://doi.org/10.1371/journal.ppat.1009534.
9. D'Arpa, P., Karna, S.L.R., Chen, T., and Leung, K.P. (2021). Pseudomonas aeruginosa transcriptome adaptations from colonization to biofilm infection of skin wounds. Sci. Rep. *11*, 20632. https://doi.org/10.1038/s41598-021-00073-4.
10. Buchanan, S.K., Smith, B.S., Venkatramani, L., Xia, D., Esser, L., Palnitkar, M., Chakraborty, R., van der Helm, D., and Deisenhofer, J. (1999). Crystal structure of the outer membrane active transporter FepA from Escherichia coli. Nat. Struct. Biol. *6*, 56–63. https://doi.org/10.1038/4931.
11. Moretti, J., Roy, S., Bozec, D., Martinez, J., Chapman, J.R., Ueberheide, B., Lamming, D.W., Chen, Z.J., Horng, T., Yeretssian, G., et al. (2017). STING Senses Microbial Viability to Orchestrate Stress-Mediated Autophagy of the Endoplasmic Reticulum. Cell *171*, 809–823.e13. https://doi.org/10.1016/j.cell.2017.09.034.
12. Ghssein, G., and Ezzeddine, Z. (2022). A review of Pseudomonas aeruginosa metallophores: Pyoverdine, pyochelin and pseudopaline. Biology *11*, 1711. https://doi.org/10.3390/biology11121711.
13. Reyes, J., Komarow, L., Chen, L., Ge, L., Hanson, B.M., Cober, E., Herc, E., Alenazi, T., Kaye, K.S., Garcia-Diaz, J., et al. (2023). Global epidemiology and clinical outcomes of carbapenem-resistant Pseudomonas aeruginosa and associated carbapenemases (POP): a prospective cohort study. Lancet. Microbe *4*, e159–e170. https://doi.org/10.1016/S2666-5247(22)00329-9.
14. Weimann, A., Dinan, A.M., Ruis, C., Bernut, A., Pont, S., Brown, K., Ryan, J., Santos, L., Ellison, L., Ukor, E., et al. (2024). Evolution and host-specific adaptation of Pseudomonas aeruginosa. Science *385*, eadi0908. https://doi.org/10.1126/science.adi0908.
15. Lee, J., and Zhang, L. (2015). The hierarchy quorum sensing network in Pseudomonas aeruginosa. Protein Cell *6*, 26–41. https://doi.org/10.1007/s13238-014-0100-x.
16. Moradali, M.F., Ghods, S., and Rehm, B.H.A. (2017). Pseudomonas aeruginosa lifestyle: a paradigm for adaptation, survival, and persistence. Front. Cell. Infect. Microbiol. *7*, 39. https://doi.org/10.3389/fcimb.2017.00039.
17. Bjarnsholt, T., Alhede, M., Alhede, M., Eickhardt-Sørensen, S.R., Moser, C., Kühl, M., Jensen, P.Ø., and Høiby, N. (2013). The *in vivo* biofilm. Trends Microbiol. *21*, 466–474. https://doi.org/10.1016/j.tim.2013.06.002.
18. Rossi, E., La Rosa, R., Bartell, J.A., Marvig, R.L., Haagensen, J.A.J., Sommer, L.M., Molin, S., and Johansen, H.K. (2021). Pseudomonas aeruginosa adaptation and evolution in patients with cystic fibrosis. Nat. Rev. Microbiol. *19*, 331–342. https://doi.org/10.1038/s41579-020-00477-5.
19. Lyu, L., Li, X., Feng, R., Zhou, X., Guha, T.K., Yu, X., Chen, G.Q., Yao, Y., Su, B., Zou, D., et al. (2023). Simultaneous profiling of host expression and microbial abundance by spatial metatranscriptome sequencing. Genome Res. *33*, 401–411. https://doi.org/10.1101/gr.277178.122.
20. Tata, M., Wolfinger, M.T., Amman, F., Roschanski, N., Dötsch, A., Sonnleitner, E., Häussler, S., and Bläsi, U. (2016). RNASeq Based Transcriptional Profiling of Pseudomonas aeruginosa PA14 after Short- and Long-Term Anoxic Cultivation in Synthetic Cystic Fibrosis Sputum Medium. PLoS One *11*, e0147811. https://doi.org/10.1371/journal.pone.0147811.
21. Mizgerd, J.P. (2003). Competing Benefits of Tumor Necrosis Factor-α for Bacteria and for Host Defense. Am. J. Respir. Crit. Care Med. *168*, 1410–1411. https://doi.org/10.1164/rccm.2310002.
22. Minns, M.S., Liboro, K., Lima, T.S., Abbondante, S., Miller, B.A., Marshall, M.E., Tran Chau, J., Roistacher, A., Rietsch, A., Dubyak, G.R., and Pearlman, E. (2023). NLRP3 selectively drives IL-1β secretion by Pseudomonas aeruginosa infected neutrophils and regulates corneal disease severity. Nat. Commun. *14*, 5832. https://doi.org/10.1038/s41467-023-41391-7.
23. Lagoumintzis, G., Xaplanteri, P., Dimitracopoulos, G., and Paliogianni, F. (2008). TNF-alpha induction by Pseudomonas aeruginosa lipopolysaccharide or slime-glycolipoprotein in human monocytes is regulated at the level of Mitogen-activated Protein Kinase activity: a distinct role of Toll-like receptor 2 and 4. Scand. J. Immunol. *67*, 193–203. https://doi.org/10.1111/j.1365-3083.2007.02053.x.
24. Narayan, K., Waggoner, L., Pham, S.T., Hendricks, G.L., Waggoner, S.N., Conlon, J., Wang, J.P., Fitzgerald, K.A., and Kang, J. (2014). TRIM13 is a negative regulator of MDA5-mediated type I interferon production. J. Virol. *88*, 10748–10757. https://doi.org/10.1128/JVI.02593-13.
25. Ahsan, N., Shariq, M., Surolia, A., Raj, R., Khan, M.F., and Kumar, P. (2024). Multipronged regulation of autophagy and apoptosis: emerging role of TRIM proteins. Cell. Mol. Biol. Lett. *29*, 13. https://doi.org/10.1186/s11658-023-00528-8.
26. Takase, H., Nitanai, H., Hoshino, K., and Otani, T. (2000). Impact of siderophore production on Pseudomonas aeruginosa infections in immunosuppressed mice. Infect. Immun. *68*, 1834–1839. https://doi.org/10.1128/IAI.68.4.1834-1839.2000.
27. Pieńko, T., and Trylska, J. (2020). Extracellular loops of BtuB facilitate transport of vitamin B12 through the outer membrane of E. coli. PLoS Comput. Biol. *16*, e1008024. https://doi.org/10.1371/journal.pcbi.1008024.
28. Hood, M.I., and Skaar, E.P. (2012). Nutritional immunity: transition metals at the pathogen-host interface. Nat. Rev. Microbiol. *10*, 525–537. https://doi.org/10.1038/nrmicro2836.
29. Lee, K.-M., Go, J., Yoon, M.Y., Park, Y., Kim, S.C., Yong, D.E., and Yoon, S.S. (2012). Vitamin B12-Mediated Restoration of Defective Anaerobic Growth Leads to Reduced Biofilm Formation in Pseudomonas aeruginosa. Infect. Immun. *80*, 1639–1649. https://doi.org/10.1128/iai.06161-11.

30. Crespo, A., Blanco-Cabra, N., and Torrents, E. (2018). Aerobic vitamin B12 biosynthesis is essential for Pseudomonas aeruginosa class II ribonucleotide reductase activity during planktonic and biofilm growth. Front. Microbiol. *9*, 986. https://doi.org/10.3389/fmicb.2018.00986.
31. Gross, F., Ring, M.W., Perlova, O., Fu, J., Schneider, S., Gerth, K., Kuhlmann, S., Stewart, A.F., Zhang, Y., and Müller, R. (2006). Metabolic engineering of Pseudomonas putida for methylmalonyl-CoA biosynthesis to enable complex heterologous secondary metabolite formation. Chem. Biol. *13*, 1253–1264. https://doi.org/10.1016/j.chembiol.2006.09.014.
32. Foglino, M., Borne, F., Bally, M., Ball, G., and Patte, J.C. (1995). A direct sulfhydrylation pathway is used for methionine biosynthesis in Pseudomonas aeruginosa. Microbiol. Read. Engl. *141*, 431–439. https://doi.org/10.1099/13500872-141-2-431.
33. Lundgren, B.R., Sarwar, Z., Pinto, A., Ganley, J.G., and Nomura, C.T. (2016). Ethanolamine Catabolism in Pseudomonas aeruginosa PAO1 Is Regulated by the Enhancer-Binding Protein EatR (PA4021) and the Alternative Sigma Factor RpoN. J. Bacteriol. *198*, 2318–2329. https://doi.org/10.1128/JB.00357-16.
34. Liu, Y., Sun, W., Ma, L., Xu, R., Yang, C., Xu, P., Ma, C., and Gao, C. (2022). Metabolic Mechanism and Physiological Role of Glycerol 3-Phosphate in Pseudomonas aeruginosa PAO1. mBio *13*, e0262422. https://doi.org/10.1128/mbio.02624-22.
35. Shibata, N., Masuda, J., Tobimatsu, T., Toraya, T., Suto, K., Morimoto, Y., and Yasuoka, N. (1999). A new mode of B12 binding and the direct participation of a potassium ion in enzyme catalysis: X-ray structure of diol dehydratase. Structure *7*, 997–1008. https://doi.org/10.1016/S0969-2126(99)80126-9.
36. Tam, E., Reno, C., Nguyen, K., Cho, S., and Sweeney, G. (2022). Importance of Autophagy in Mediating Cellular Responses to Iron Overload in Cardiomyocytes. Rev. Cardiovasc. Med. *23*, 167. https://doi.org/10.31083/j.rcm2305167.
37. Chadha, J., Harjai, K., and Chhibber, S. (2022). Revisiting the virulence hallmarks of Pseudomonas aeruginosa: a chronicle through the perspective of quorum sensing. Environ. Microbiol. *24*, 2630–2656. https://doi.org/10.1111/1462-2920.15784.
38. Mukhopadhyay, S., Encarnación-Rosado, J., Lin, E.Y., Sohn, A.S.W., Zhang, H., Mancias, J.D., and Kimmelman, A.C. (2023). Autophagy supports mitochondrial metabolism through the regulation of iron homeostasis in pancreatic cancer. Sci. Adv. *9*, eadf9284. https://doi.org/10.1126/sciadv.adf9284.
39. Wilson, B.R., Bogdan, A.R., Miyazawa, M., Hashimoto, K., and Tsuji, Y. (2016). Siderophores in Iron Metabolism: From Mechanism to Therapy Potential. Trends Mol. Med. *22*, 1077–1090. https://doi.org/10.1016/j.molmed.2016.10.005.
40. Tsalamandris, G., Hadjivassiliou, M., and Zis, P. (2023). The Role of Nutrition in Neurological Disorders. Nutrients *15*, 4713. https://doi.org/10.3390/nu15224713.
41. Zhou, H., Negrón, O., Chumbler, N., Mihaela, G., and Pearlman, E. (2024). Spatial Transcriptomics Datasets : P. aeruginosa Corneal Infection (Zenodo). https://doi.org/10.5281/zenodo.14497751.
42. Stover, C.K., Pham, X.Q., Erwin, A.L., Mizoguchi, S.D., Warrener, P., Hickey, M.J., Brinkman, F.S., Hufnagle, W.O., Kowalik, D.J., Lagrou, M., et al. (2000). Complete genome sequence of Pseudomonas aeruginosa PAO1, an opportunistic pathogen. Nature *406*, 959–964. https://doi.org/10.1038/35023079.
43. Liberati, N.T., Urbach, J.M., Miyata, S., Lee, D.G., Drenkard, E., Wu, G., Villanueva, J., Wei, T., and Ausubel, F.M. (2006). An ordered, nonredundant library of Pseudomonas aeruginosa strain PA14 transposon insertion mutants. Proc. Natl. Acad. Sci. USA *103*, 2833–2838. https://doi.org/10.1073/pnas.0511100103.
44. Schneider, C.A., Rasband, W.S., and Eliceiri, K.W. (2012). NIH Image to ImageJ: 25 years of image analysis. Nat. Methods *9*, 671–675. https://doi.org/10.1038/nmeth.2089.
45. Sievers, F., and Higgins, D.G. (2014). Clustal Omega. Curr Protoc Bioinformatics. *48*, 3.13.1–3.13.16. https://doi.org/10.1002/0471250953.bi0313s48.
46. Gutierrez, S., Tyczynski, W.G., Boomsma, W., Teufel, F., and Winther, O. (2022). MembraneFold: Visualising transmembrane protein structure and topology. Preprint at bioRxiv. https://doi.org/10.1101/2022.12.06.518085.
47. Rosignoli, S., and Paiardini, A. (2022). Boosting the Full Potential of PyMOL with Structural Biology Plugins. Biomolecules *12*, 1764. https://doi.org/10.3390/biom12121764.
48. Trott, O., and Olson, A.J. (2010). AutoDock Vina: Improving the speed and accuracy of docking with a new scoring function, efficient optimization, and multithreading. J. Comput. Chem. *31*, 455–461. https://doi.org/10.1002/jcc.21334.
49. Muzellec, B., Teleńczuk, M., Cabeli, V., and Andreux, M. (2023). PyDESeq2: a python package for bulk RNA-seq differential expression analysis. Bioinformatics *39*, btad547. https://doi.org/10.1093/bioinformatics/btad547.
50. Klopfenstein, D.V., Zhang, L., Pedersen, B.S., Ramírez, F., Warwick Vesztrocy, A., Naldi, A., Mungall, C.J., Yunes, J.M., Botvinnik, O., Weigel, M., et al. (2018). GOATOOLS: A Python library for Gene Ontology analyses. Sci. Rep. *8*, 10872. https://doi.org/10.1038/s41598-018-28948-z.
51. Arora, I., Kummer, A., Zhou, H., Gadjeva, M., Ma, E., Chuang, G.-Y., and Ong, E. (2024). mtx-COBRA: Subcellular localization prediction for bacterial proteins. Comput. Biol. Med. *171*, 108114. https://doi.org/10.1016/j.compbiomed.2024.108114.
52. Ong, E., Wang, H., Wong, M.U., Seetharaman, M., Valdez, N., and He, Y. (2020). Vaxign-ML: supervised machine learning reverse vaccinology model for improved prediction of bacterial protective antigens. Bioinforma. Oxf. Engl. *36*, 3185–3191. https://doi.org/10.1093/bioinformatics/btaa119.
53. Singh, P.K., Singh, S., Wright, R.E., III, Rattan, R., and Kumar, A. (2020). Aging, But Not Sex and Genetic Diversity, Impacts the Pathobiology of Bacterial Endophthalmitis. Investig. Ophthalmol. Vis. Sci. *61*, 5. https://doi.org/10.1167/iovs.61.14.5.
54. Turner, K.H., Everett, J., Trivedi, U., Rumbaugh, K.P., and Whiteley, M. (2014). Requirements for Pseudomonas aeruginosa Acute Burn and Chronic Surgical Wound Infection. PLoS Genet. *10*, e1004518. https://doi.org/10.1371/journal.pgen.1004518.
55. Capra, J.A., and Singh, M. (2007). Predicting functionally important residues from sequence conservation. Bioinformatics *23*, 1875–1882. https://doi.org/10.1093/bioinformatics/btm270.
56. van Kempen, M., Kim, S.S., Tumescheit, C., Mirdita, M., Lee, J., Gilchrist, C.L.M., Söding, J., and Steinegger, M. (2024). Fast and accurate protein structure search with Foldseek. Nat. Biotechnol. *42*, 243–246. https://doi.org/10.1038/s41587-023-01773-0.

STAR★METHODS

KEY RESOURCES TABLE

REAGENT or RESOURCES	SOURCE	IDENTIFIER
Antibodies		
PanCK	Invitrogen	Clone:AE1 + AE3 Cat:PA5-144555RRID:AB_2935724
OprI	Thermo Fisher Scientific	Opr17_VHHFC RRID:AB_3092372
Ly6G	Novus Biologicals	Clone: 1A8 NB253131AFD PRID:AB2572720
cKit	Novus Biologicals	Clone: 9D2 NB110-93600AF532 PRID: AB_3181352
Bacterial and virus strains		
P. aeruginosa PAO1	Stover et al.[42]	https://doi.org/10.1038/35023079
P. aeruginosa PA14	Liberati et al.[43]	https://doi.org/10.1073/pnas.0511100103
P. aeruginosa PA14 PA2590Tn	Liberati et al.[43]	https://doi.org/10.1073/pnas.0511100103
Chemicals, peptides, and recombinant proteins		
Luria–Bertoni broth	BD-Difco	Cat# 244620
10XPBS	Sigma Aldrich	Cat# 5368
Ketamine HCl (100 mg/ml)	MWI Animal Health	Cat# 501072
Xylazine (XylaMed)	MWI Animal Health	Cat# 119711
Luria–Bertoni Agar	BD Difco	Cat# 244520
10% formalin	Thermo Fisher	Cat# SF100-4
Proteinase K	Thermo Fisher	Cat# AM2548
100% deionized formamide	Thermo Fisher	Cat# AM9342
20xSSC	Invitrogen	Cat# AM9763
10% Tween 20	Teknova	Cat# T0710
1X EDTA pH 9.0	Sigma Aldrich	Cat# SKU SRE0063
100% Ethanol	Fisher Chemical	Cat# CAS64-17-5
Tris Base	Fisher Bioreagents	Cat# BP150-500
Elution buffer (10 mM Tris-HCl w 0,05 Tween 20, pH8.0	Teknova	Cat# T1485
Bond Dewax solution	Leica Biosystems	Cat# AR9222
Bond TM epitope retrieval 2	Leica Biosystems	Cat# AR9640
GeoMx DSP RNA slide FFPE prep kit (Contains Buffer W, Buffer R)	NanoString Technologies	Cat# 121300313
SYTO13	Invitrogen	Cat# S11364
GeoMx morphology kit	NanoString Technologies	Cat# SH003
Invitrogen Qubit quantification assay kit	Invitrogen	Cat #Q32854
DEPC-Treated Water	Invitrogen	Cat #43-879-37
Deposited data		
Transcriptomics raw data and associated images	This paper	NCBI Project Accession: PRJNA1202130; Zenodo Record: https://zenodo.org/records/14667250
Code	This paper	The analysis code is available at GitHub (https://github.com/modernatx/spatial_RNAseq_analyses) and has also been archived on Zenodo (https://zenodo.org/records/14667250) for reproducibility.
Experimental models: Organisms/strains		
C57BL6/J	The Jackson Laboratory	Cat# 000664

(*Continued on next page*)

Continued

REAGENT or RESOURCES	SOURCE	IDENTIFIER
Oligonucleotides		
Probes targeting 100 P. aeruginosa genes	This paper	Table S1
GeoMx NGS RNA WTA	NanoString Technologies	Cat #12141103
Software and algorithms		
ImageJ	Schneider et al.[44]	https://imagej.nih.gov/ij/
Clustal Omega	Sievers and Higgens[45]	https://bio.tools/clustalo
MembraneFold	Gutierrez et al.[46]	https://biolib.com/KU/MembraneFold/
PyMOL v2.5.4	Rosignoli and Paiardini[47]	https://www.pymol.org/
Autodock Vina	Trott and Olson[48]	https://vina.scripps.edu/
DESeq2	Muzellec et al.[49]	https://bioconductor.org/packages/release/bioc/html/DESeq2.html
GOATools	Klopfenstein et al.[50]	https://github.com/tanghaibao/goatools
GeoMxNGSPipeline v.2.3.3.10	NanoString Technologies	
mtx-COBRA	Arora et al.[51]	https://doi.org/10.1016/j.compbiomed.2024.108114
Vaxign-ML	Ong et al.[52]	https://doi.org/10.1093/bioinformatics/btaa119
BioRender		https://BioRender.com
Other		
GeoMx Seq Code Pack_ABCD (comes with Master Mix)	NanoString Technologies	Cat# 121400205
GeoMx Seq Code Pack_EFGH (comes with Master Mix)	NanoString Technologies	Cat# 121400206
GeoMx DSP Collection Plate 96	NanoString Technologies	Cat# 100473
RNase/DNase free 96-well PCR plates	Thermo Scientific	AB-1400-L
AMPure XP beads	Beckman Coulter	NC9933872

EXPERIMENTAL MODEL AND STUDY PARTICIPANT DETAILS

Healthy, naive C57BL/6J (WT) mice, aged 6–8 weeks, were purchased from the Jackson Laboratory (Bar Harbor, ME, cat #000664) and were housed in a UC Irvine IACUC approved facility. B-level holding rooms, where mice were housed prior to infection, are kept between 70 and 72°C with a humidity of 50–55%. The mice used in the study were not subject to previous procedures. For the keratitis model of infection, mice are transferred to a Department of Ophthalmology procedure room containing approved anesthesia methods and recovery equipment. Once mice are infected and have recovered from anesthesia, they are transferred to a D-level holding room with the same temperature and humidity settings as described prior. At experimental endpoints, mice are euthanized by CO_2 asphyxiation followed by approved secondary euthanasia method of cervical dislocation. Infected carcasses are collected by the UC Irvine animal facility Environmental Health and Safety department and are incinerated in accordance with local regulations.

For each experiment, mice were purchased in cohorts of 25–50 at a time and experiments were conducted using mice of the same ordered cohort. According to the Jackson Laboratory's analysis on weight, mice aged 6–8 weeks were between 15g and 25g. We used both sexes as we found no differences in the corneal infections. Studies in bacterial endophthalmitis which share similarities to keratitis highlight impact of age rather than sex on disease outcomes.[53]

Mice were housed at five animals per cage with no special diet or cage space. All animal procedures and housing requirements were approved by the UC Irvine IACUC under protocol AUP-21-123.

Overnight cultures of *P. aeruginosa* were grown to an OD_{600} of 0.20 in LB broth, and cultures were then washed and resuspended in 1x sterile PBS (Corning). C57BL/6J mice were anesthetized with ketamine/xylazine (MWI Animal Health) and corneal epithelium was abraded with three, parallel 10mm scratches, performed with a 26 ½ -gauge needle (BD). *Pseudomonas* was then applied to the abraded cornea topically with 2μL containing 5×10^5 CFU in PBS in the PA14 infection studies and with 5mL of 1×10^6 CFU in the PAO1 infection studies. For use in the infection experiments, 100μL of overnight culture was added to 10mL of fresh LB and was subcultured for 2.5-3h to reach $OD_{600} = 0.20$. 1mL of culture was spun down at 3,000 x g (rotor, centrifuge) for 10 min and diluted to a desired inoculum. Experiments were carried out predominantly with male 7–8 week old C57Bl6/J mice and repeated twice. The infection studies were carried out with $N = 5$ mice/cohort/experiment. Experiments were repeated twice or thrice without blinding at any stage of the study. Sample sizes were estimated based on prior experience. Exclusion criteria included cases where animals presented with wounding or corneal opacity in the eye that was not caused by infection.

METHOD DETAILS

Bacterial strains

P. aeruginosa strains PAO1, PA14, PA14_30590_Tn (PA2590 transposon mutant) were grown in Luria–Bertoni broth (LB) broth (BD-Difco) overnight at 37°C with agitation (200rpm). Cultures were then passaged in fresh LB broth (BD-Difco) until an OD_{600} of 0.20 (midlog phase) was reached. The PAO1 strain was obtained from Dr. A. Rietsch (Case Western Reserve University).[42] The PA14 and PA14_2590_Tn were generated during the PA14 transposon insertion mutant library generation ((http://ausubellab.mgh.harvard.edu/cgi-bin/pa14/home.cgi)) and obtained from Prof. G. Pier (Brigham and Women's Hospital, Harvard Medical School).[43] The PA2590 transposon mutant was sequence validated (data not shown).

Corneal opacity

Corneal images were recorded from infected C57Bl6/J mice at either 24h or 48h post *P. aeruginosa* challenges. Corneal images were taken using a Leica MZ10 F Modular Stereo Microscope with a Leica DFC450 C camera attachment. Image brightness was adjusted manually using ImageJ software (NIH) and was kept consistent for all images. Images were then converted to 8-bit for quantification.[44] Using ImageJ, ROIs were drawn around the corneal area only (excluding the sclera) and mean intensity was recorded for each ROI. Images were corrected by subtracting intensity caused by glare of dissection lights (glare values were based on naive corneas). Percent corneal opacity was calculated by dividing corrected mean intensity by the intensity of a completely white cornea.

Bacterial quantification

Once images were taken, eyes were resected and corneas placed into a 2 mL centrifuge tube containing 1mL of sterile 1x PBS and a sterile steel ball bearing (5 mm diameter). Tubes were placed in a Qiagen Tissue Lyser II and were homogenized at 30Hz for 3 min. After lysis, homogenates were serially diluted up to 1:10,000 and 10μL of each dilution was plated onto one LB agar (BD-Difco) plate (concentrations plated: undiluted, 1:10, 1:100, 1:1,000, 1:10,000). Dilutions were streaked down the plate and plates were incubated at 37°C with 5% CO_2 overnight and colony forming units (CFU) were counted manually the next day. CFU was then quantified as CFU/ml.

Ocular tissue processing

Separate cohorts of naive and infected mice were used to source ocular tissues for spatial transcriptome analysis. These cohorts comprised mice infected with either PAO1 or PA14 harvested at either 24h or 48h post-challenges. After imaging the corneas, eyes had 15μL of 4% formalin (ThermoFisher) dropped onto them and were left to fix at room temperature for 15 min. Eyes were then carefully resected and placed in 1mL of iced 4% formalin (ThermoFisher) and were fixed at 4°C for 48-72hrs. After fixation, formalin was removed, and tissue was washed twice with sterile 1x PBS. Samples were then placed in 2mL of 70% ethanol and were kept at 4°C until shipment to UMass Histopathology was complete. Tissue embedding was done by UMass Histopathology. All tissues were processed using UMass Chan Medical School Morphology Core services following standard protocols.

Spatial transcriptomics workflow

Target selection and probe designs

Probes targeting 100 selected genes in the PAO1 strain of *P. aeruginosa* were designed using Nanostring in-house scripts (Table S1). The 100 bacterial transcripts were selected based on comparative genomics analysis and sequence conservation analysis across cystic fibrosis, urinary tract infections, and ocular infections. We also considered surface exposure predictions (extracellular and outer membrane) (MTX-COBRA), immunogenicity predictions (Vaxign ML),[51],[52] and previous reports demonstrating *in vivo* transcription.[2],[8],[54] Lastly, we included genes with known functional importance for *P. aeruginosa* virulence. The probes were designed to specifically bind to *Pseudomonas* genes, avoiding cross-reactivity with mouse genes and other microbes leveraging Nanostring in-house scripts.

Tissue processing for spatial transcriptomics

5um sections from formalin-fixed paraffin embedded (FFPE) tissue blocks were mounted onto Superfrost Plus slides and prepped for GeoMx spatial transcriptomic profiling. Briefly, slides were baked at 60°C for 1 h prior to loading on a BOND RXm (Leica Biosystems). Once loaded, the BOND RXm will bake the slides for 30 min at 60°C, dewax with 150uL of Bond Dewax Solution (Leica Biosystems) for 30 s 5 times at 72°C and rehydrate with 150uL of reagent-grade ethanol (Leica Biosystems) 3 times at RT. BOND RXm will then perform heat-induced epitope retrieval with Bond ER Solution (Leica Biosystems) for 20 min at 100°C followed by enzymatic digestion with 0.1 μg/mL proteinase K (Thermo Fisher) for 15 min at 37°C. Enzymatic digestion was stopped with 10% Neutral Buffered Formalin for 5 min at RT followed by NBF Stop Buffer (0.1M tris, 0.1M glycine in DEPC-treated water) for 5 min at RT. Slides were removed from BOND RXm upon run completion and tissue sections were then hybridized with 25 μL Nanostring mouse Whole Transcriptome Atlas (GeoMx NGS RNA WTA, Nanostring Technologies) and 12.5 μL custom *P. aeruginosa* probes (Nanostring Technologies) in 200 μL Buffer R (Nanostring Technologies) media in 250 μL total volume per slide at 37° overnight. Following hybridization, two, 25min stringency washes with a 1:1 mix of 100% deionized formamide (Thermo Fisher) and 4X SSC (Invitrogen) were performed to remove off-target probes. Sections were subsequently blocked with 200 μL Buffer W (Nanostring Technologies) for 30 min in a humidified chamber at RT and stained with the following morphology marker antibodies: DNA (Syto13; 488 channel; Nanostring), PanCK (532 channel; GeoMx morphology kit, Nanostring), OprI (Opr17_VHHFC; 594 channel; Thermo Fisher Scientific) or cKit (92D; 594 channel; Novus Biologicals), and Ly6G (1A8; 647 channel; Novus Biologicals) in a total volume of 200 μL in Buffer W media for 1h in a humidified chamber at RT. OprI antibody was conjugated to Alex Fluor 594 using the Molecular Probes Alexa Fluor Antibody Labeling Kit (ThermoFisher). Slides were then loaded into the GeoMx DSP instrument where the entire sections were scanned and imaged. Regions of interest (ROIs) were manually drawn on the section images to capture corneal epithelial ROIs, stromal ROIs, and anterior chamber ROIs. Three ROIs per epithelial, stromal, and anterior chamber tissue segments were selected for each ocular cross section. The GeoMx DSP then directed UV light to each ROI to cleave the barcodes (RNA ID and unique molecular identifier-containing oligonucleotide) from the bound probes. The collection plate (GeoMx DSP Collection plate 96, Nanostring) is sealed with a permeable membrane and dried down on a thermocycler at 65°C for 1h or stored at −20°C for up to 30 days. After the dry down, the permeable seal is replaced with a new permeable membrane, plate is spun down to ensure lack of remaining liquid. The plate is then rehydrated with 10 μL DEPC water for 10 min at RT.

Illumina i5 and i7 dual-indexing primers (Nanostring Technologies) were added to the collected barcodes during polymerase chain reaction (8 μL collected oligonucleotides/ROI) to uniquely index each ROI. Briefly, collected barcodes were re-suspended in 10 μL of nuclease-free water and incubated for 10 min at room temperature. In a 96-well PCR plate, 2 μL of master mix (Nanostring Technologies), 4 μL of seq-code indexes (GeoMx Seq code pack, Nanostring Technologies) and 4 μL of re-suspended barcodes were mixed and placed in a thermocycler for PCR amplification using the following program. 1x UDG incubation for 30 min at 37°C, 1x UDG deactivation for 10 min at 50°C, 1x Initial denaturation for 3 min at 95°C, 18x Denaturation for 15 s at 95°C > Anneal for 60 s at 65°C > Extend for 30 s at 68°C, Final extension for 5 min at 68°C, Hold at 4°C.

Once the PCR program was completed, 6 μL of the no-template control (NTC; well A1) was added to an Eppendorf tube and 8 μL of each remaining well was pooled. AMPure XP beads (Beckman Coulter) were used for purification of PCR. Briefly, 1.2x volume of AMPure XP beads was added to NTC and pool tubes and incubated at room temperature for 5min followed by an additional 5min incubation on a DynaMag-2 magnetic stand (Thermo Fisher). While still on the magnetic stand, liquid was discarded from the tubes and the magnetic bead pellets washed 2x with 80% Ethanol for 30s each time, then allowed to air dry for 5min. The library was eluted from the AMPure XP beads by adding 54 μL of elution buffer (Tris-HCl 10mM w/0.05% Tween 20, pH 8.0; Teknova) to each tube followed by pelleting beads on the magnetic stand for 5min 50 μL of each elution was transferred to a new tube and 60 μL of AMPure XP beads added. Tubes were incubated at room temperature for 5min and beads pelleted on the magnetic stand for 5min. Liquid was removed and pellets washed again 2x with 80% Ethanol and allowed to air dry for 5min.

For the final elution, 5uL of elution buffer was added to the NTC tube and 12uL added to the library tube(s) and incubated at room temperature for 5min, then pelleted on the magnetic stand for 5min 4 μL from the NTC tube and 11 μL from the library tube(s) was transferred to a new tube to generate the final purified library. Library concentration was measured using a Qubit fluorimeter (ThermoFisher Scientific) using the high-sensitivity dsDNA kit (Invitrogen), and quality was assessed using a Tape Station (Agilent Technologies).

Illumina sequencing and sequence data processing

The sequencing depth requirement was determined by aggregating the areas of illumination (measured in μm^2) and multiplying the total area by a factor of 100, as recommended in the GeoMx DSP Library and Sequencing Guide (nanostring.com). Sequencing was executed using the NovaSeq 6000 System. The resultant FASTQ files were processed to Digital Count Conversion (DCC) files utilizing the GeoMxNGSPipeline v.2.3.3.10, a pipeline publicly available through NanoString Technologies. This pipeline facilitated individual probe alignment by identifying read tag sequences (RTS). Additionally, it eliminated duplicates in probe counts generated during the library preparation's polymerase chain reaction, through a meticulous analysis of the unique molecular identifiers (UMIs) associated with each probe.

QUANTIFICATION AND STATISTICAL ANALYSIS

Bacterial burden and opacity statistical analysis

Data are represented as mean ± SD values and analyzed via unpaired two-sided Student's t test with Welch's correction using GraphPad Prism v10.4.1 software. The number of animals, N, included in the analysis is listed under each figure legends section.

Spatial transcriptome analysis

The DCC files underwent analysis using NanoString Technologies' GeoMx Digital Spatial Profiler. Key metrics such as the number of raw reads, the alignment rate of these reads, and the sequencing saturation for each area of illumination were scrutinized to evaluate the quality of library preparation. Criteria for inclusion in the analysis were set: more than 10^6 raw reads per ROI, an alignment rate exceeding 80%, and a sequencing saturation greater than 80%. A "no template control" sample, devoid of target probes, was integrated into the library preparation and subsequent sequencing to gauge potential contamination. To estimate background noise and determine the limit of quantification, negative control probes employing External RNA Controls Consortium (ERCC) sequences were included in each GeoMx RNA assay. Target probe data were filtered based on frequency within each ROI, followed by normalization against the highest negative control counts using background subtraction. Differential gene expression analysis across various groups was performed using DESeq2, a statistical method designed to identify significant changes in normalized gene expression levels.[49] The Python-based library GOATools were used for the functional enrichment analysis.[50]

Predictive models and correlative analysis

We employed Random Forest (RF), Ridge Regression (RR), and Support Vector Machine (SVM) algorithms for predictive analysis, with these models trained on a complete set of host features (as detailed in Figure S3A). We utilized a 5-fold cross-validation approach on spatially resolved host gene expression profiles across infected tissue regions. For each model, data from the ROIs across different infected tissues served as individual observations. This cross-validation was further extended to account for biological variability by training on all but one host (leave-one-out validation) to ensure that predictions could generalize to different hosts. Among these, Ridge Regression emerged as the most accurate model and was selected for further in-depth analysis and optimization.

The Ridge Regression model was trained using host response profiles and subsequently used to predict the expression data of the PA *rplL* gene. For normalization of data values, a log transformation ($\log_2$(values +1)) was applied. To assess the model's predictive accuracy, we implemented a 5-fold cross-validation strategy, utilizing Regions of Interest (ROIs) from mice that had been infected. Additionally, cross-validation was carried out across different hosts to validate the model's capacity to predict outcomes in hosts at similar infection stages, as detailed in Figure S2. The effectiveness of the model was thoroughly evaluated based on the average Mean Absolute Error (MAE), Explained Variance Score (EVS), and R^2 scores.

Further, we assessed the model's performance when trained with varying numbers of mouse gene features. For this, we selected the top-performing features based on their coefficient values in the model trained with the complete dataset. The primary metric for assessing these subset-trained models was the average R^2 score. To optimize these models, based on different sets of features, we applied a grid search technique for hyperparameter tuning, ensuring that each model was fine-tuned for the best possible predictive performance.

We assessed correlations between bacterial *rplL* and host gene expressions using Spearman's rank correlation, with *p*-value adjustments made through the Benjamini-Hochberg FDR method.

PA2590 sequence analysis

To identify the PA2590 gene, we analyzed more than 11,000 genome sequences from clinical isolates collected between 2000 and 2023. These sequences, sourced from the NCBI database, were subjected to BlastP analysis with the criteria of >85% identity and >70% query and >70% subject coverage, to identify homologous genes of PA2590. Following this, Clustal Omega was utilized for sequence alignment.[45] The conservation of amino acid residues within PA2590 was quantitatively evaluated using Shannon Entropy.[55] This approach effectively highlights conserved regions by examining the variability of amino acid positions across the aligned sequences, offering insights into the evolutionary stability of the gene. MembraneFold was employed to predict membrane topology of PA2590.[46]

Structural homology analysis and molecular docking

For structural insights, we employed Foldseek to align PA2590 (www.uniprot.org/uniprotkb/Q9I0P7/entry#structure) with existing structures in the Protein DataBank (PDB) in 01/2024.[56] This alignment was instrumental in hypothesizing the functional structure of PA2590, based on similarities with known protein structures. Structural superimposition was conducted using the cmd.align function in PyMOL v2.5.4, involving 1000 alignment cycles with the transform parameter set to 1.[47] *In silico* docking experiments were conducted using Autodock Vina.[48] The pose with the lowest energy score (kcal/mol) was chosen for representation. Pymol scripts were used to highlight residues potentially interacting with PA2590, focusing on polar contacts within a 3.5 Å range.